GRANT

IN-91-CR

28595

p. 44

Semiannual Status Report

NASA-Ames Cooperative Agreement Number NCC 2-680

DIURNAL FORCING OF PLANETARY ATMOSPHERES

For the period January 1 through June 30, 1991

Submitted to

Dr. Robert M. Haberle, Technical Officer
National Aeronautics and Space Administration
Ames Research Center, MS 245-3
Moffett Field, California 94035

Prepared by

Dr. Howard C. Houben, Principal Investigator
Space Physics Research Institute
572 Hyannis Drive
Sunnyvale, California 94087-1315
(408) 736-9705

(NASA-CR-188779) DIURNAL FORCING OF PLANETARY ATMOSPHERES Semiannual Status Report, 1 Jan. - 30 Jun. 1991 (Space Physics Research Inst.) 44 p CSCL 03B

N91-31056

Unclas
G3/91 0038295

Progress Report

The utility of the Mars Planetary Boundary Layer Model (MPBL) for calculations in support of the Mars 94 balloon mission has been substantially enhanced by the introduction of a balloon equation of motion into the model. Both vertical and horizontal excursions of the balloon are calculated along with its volume, temperature, and pressure. The simulations reproduce the expected 5-minute vertical oscillations of a constant density balloon at altitude on Mars. Figures 1-3 show the results of these calculations for the nominal target location of the balloon (latitude 50 degrees; solar longitude 170 degrees; thermal inertia 360 SI; visible optical depth 0.45; infrared optical depth 0.30; surface albedo 0.20; surface pressure 600mb) referred to as Moyen 50m by the French and Russians.

Papers giving full details of the MPBL and its coupling to the Martian regolith for water vapor transport calculations are now in preparation. A paper entitled "A coupled subsurface atmosphere boundary layer model of H_2O on Mars" by A. P. Zent, R. M. Haberle, H. Houben, and B. M. Jakosky was presented at the 22nd Lunar and Planetary Science Conference in March. The abstract is attached as Appendix A.

A nonlinear balanced model (renamed the Balance System Model to emphasize the fact that a full dynamically-consistent set of equations is solved, rather than just the balance equation) has been developed for the Martian atmosphere. This model takes temperature data (such as are to be expected from satellite missions) and computes dynamically consistent rotational wind fields, diabatic heating rates, and diabatic circulations. Results of this model have been compared with those from the full primitive equation model calculations of the Mars Climate Model (MCM) under both clear and dusty conditions. The accompanying Figures 4-7 illustrate the Balance System Model's ability to diagnose winds using only information about the mass field.

The Balance System Model has been used to initialize a primitive equation model for simulations of the earth's stratosphere at the time of the El Chichon eruption in 1982. (The available satellite observations include only the temperatures and thus closely resemble the expected Martian observations.) As is the case with many such model simulations, a cold pole develops over time--probably due to the inadequate representation of small-scale gravity waves. Therefore, the Balance System Model is used as an assimilation model to update the temperature and wind fields at frequent intervals. The results for May and June (the third and fourth months of the simulation) are illustrated in Figures 8-15.

Future Work

Along with the completion of the papers now in preparation, work on the MPBL will emphasize those elements needed to further delineate the slope wind model. In particular, a self-consistent pressure calculation, while computationally unwieldy, should allow a better forecast of slope winds (possibly even involving complex terrains in a 2-dimensional model). This improved modeling, along with further study of the newly available

topography and figure data for Mars, should result in better simulations of the Viking Lander meteorological data. Of particular concern is the very strong vertical wind shear inferred from the Viking entry science.

It is expected that further extensions of the current suite of Mars models to the other terrestrial planets will be undertaken in the near future. Of particular interest is the planet Venus, where recent spacecraft missions (Galileo and Magellan) have generated much excitement about that planet's atmosphere and surface-atmosphere interactions.

Figure Captions

Figure 1. MPBL results for the nominal target point of the Mars 94 balloon mission. (See text for particulars.) Plotted as functions of time of day are balloon altitude, balloon and ambient temperatures, and balloon and ambient pressures.

Figure 2. Further MPBL results using the balloon equation of motion. The vertical velocity and balloon overpressure plots show clear indications of the 5 minute vertical oscillation which is characteristic of a constant volume balloon under mars conditions.

Figure 3. The horizontal displacement of the balloon as a function of time of day (symbols are plotted every hour) based on the above MPBL calculations. A significant fraction of the balloon's travel takes place at night while it is "parked" at low altitude in spite of the frictional drag which must be considered under those circumstances.

Figure 4. A comparison of winds generated by a 3-D primitive equation model of the Martian atmosphere (MCM) in a dust-free simulation with the winds diagnosed by the Balance System Model using only the temperature fields of the MCM. a) The zonal mean temperature field of the MCM; b) the diagnosed diabatic heating rates (degrees per day) in the atmosphere; c) the MCM mean zonal wind; and d) the mean zonal wind diagnosed by the Balance System Model based only on the temperatures in (a).

Figure 5. A continuation of the comparison between the MCM and the Balance System Model in a dust-free atmosphere. a) The mean meridional circulation of the MCM (the density-weighted streamlines shown are in units of 0.1 megatons/second of material transport across a latitude circle); b) the mean meridional circulation diagnosed by the Balance System Model; c) streamlines of the horizontal flow for the MCM (units are m/s) at the 3mb pressure level; and d) the corresponding streamlines of the Balance System model.

Figure 6. Another comparison between the MCM and Balance System Model as in Fig. 4, but for a dusty atmosphere with optical depth 1.

Figure 7. As in Fig. 5, but for dust optical depth 1.

Figure 8. A comparison between the observed average stratospheric temperatures in May 1982 (from the National Meteorological Center) and 3-D model calculations. Since the mean temperature field in the model is updated using the Balance System Model as an assimilation routine, this figure illustrates the drift between model and observed temperatures over a period of 24 hours.

Figure 9. a) The computed mean zonal wind in the stratosphere in May 1982. This quantity is not directly observed. The developing south polar night jet and the summer hemisphere easterly mesospheric jet are quite evident. b) The computed mean meridional wind in the stratosphere in May 1982. All winds are quite light except in the highly viscous sponge layer near the top of the model. Units are m/s.

Figure 10. A comparison between modeled and observed geopotential height fields in the stratosphere in May 1982 for zonal wavenumber one. The model generally shows larger amplitudes than the observations, but agreement below 10mb (the region of greatest interest for considerations of transport of the El Chichon cloud) is good.

Figure 11. A comparison between modeled and observed geopotential height fields in the stratosphere in May 1982 for zonal wavenumber 2. There is some indication in the observations of instability of the polar night jet at high altitudes. Strong friction in the model at these heights damps any such instabilities.

Figure 12. As in Fig. 8, for June 1982.

Figure 13. As in Fig. 9, for June 1982. The polar night jet is continuing to accelerate, consistent with climatological data.

Figure 14. As in Fig. 10, for June 1982.

Figure 15. As in Fig. 11, for June 1982. In this plot there is the hint that the instability of the polar night jet is overcoming even the strong damping of the model sponge layer.

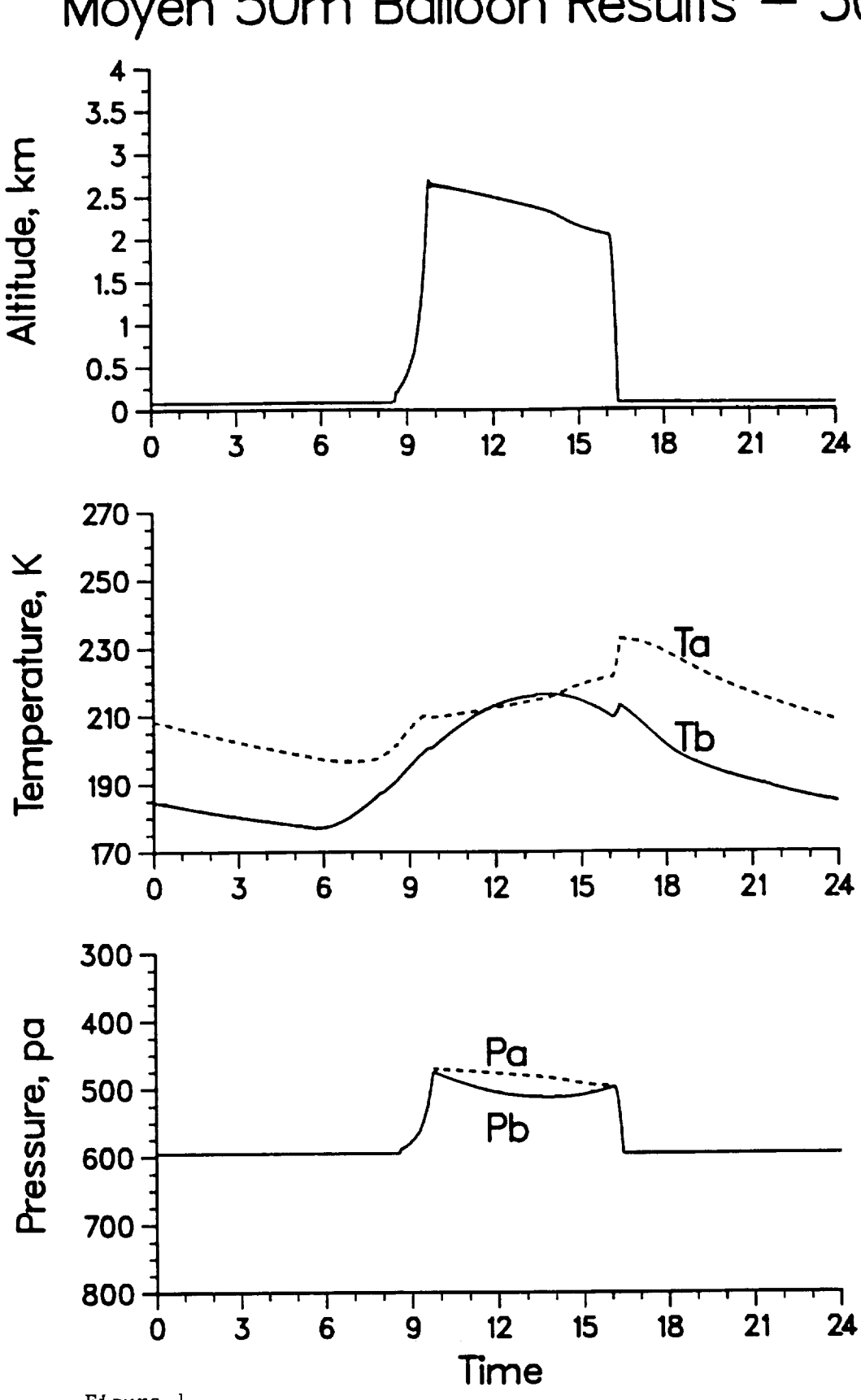
Moyen 50m Balloon Results – 50N
Altitude, km
4
3.5
3
2.5
2
1.5
1
0.5
0
0
3
6
9
12
15
18
21
24
Temperature, K
270
250
230
210
190
170
Ta
Tb
Pressure, pa
300
400
500
600
700
800
Pa
Pb
Time

Figure 1.

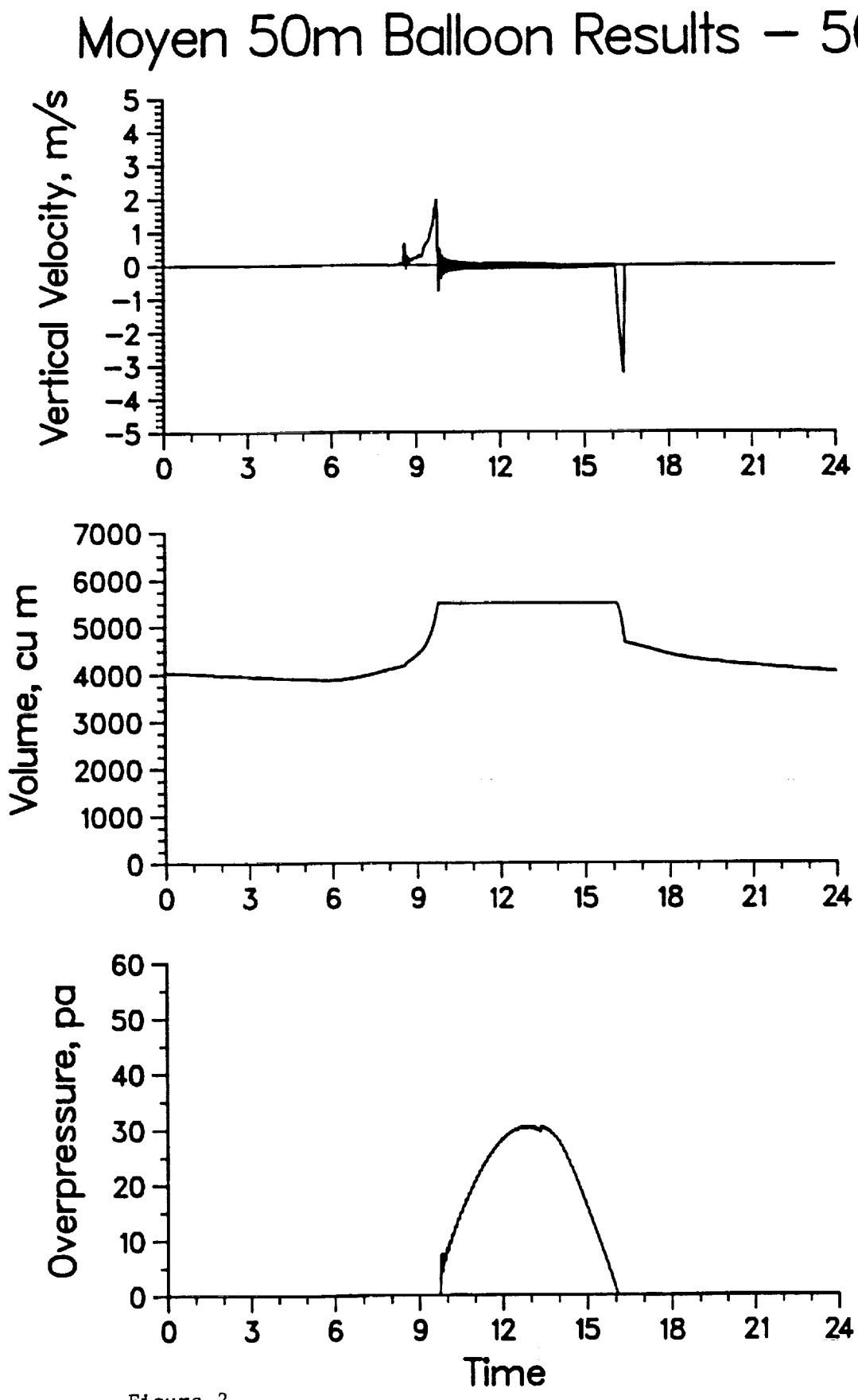
Moyen 50m Balloon Results – 50N
Vertical Velocity, m/s
5
4
3
2
1
0
-1
-2
-3
-4
-5
0
3
6
9
12
15
18
21
24
Volume, cu m
7000
6000
5000
4000
3000
2000
1000
0
Overpressure, pa
60
50
40
30
20
10
0
Time

Figure 2.

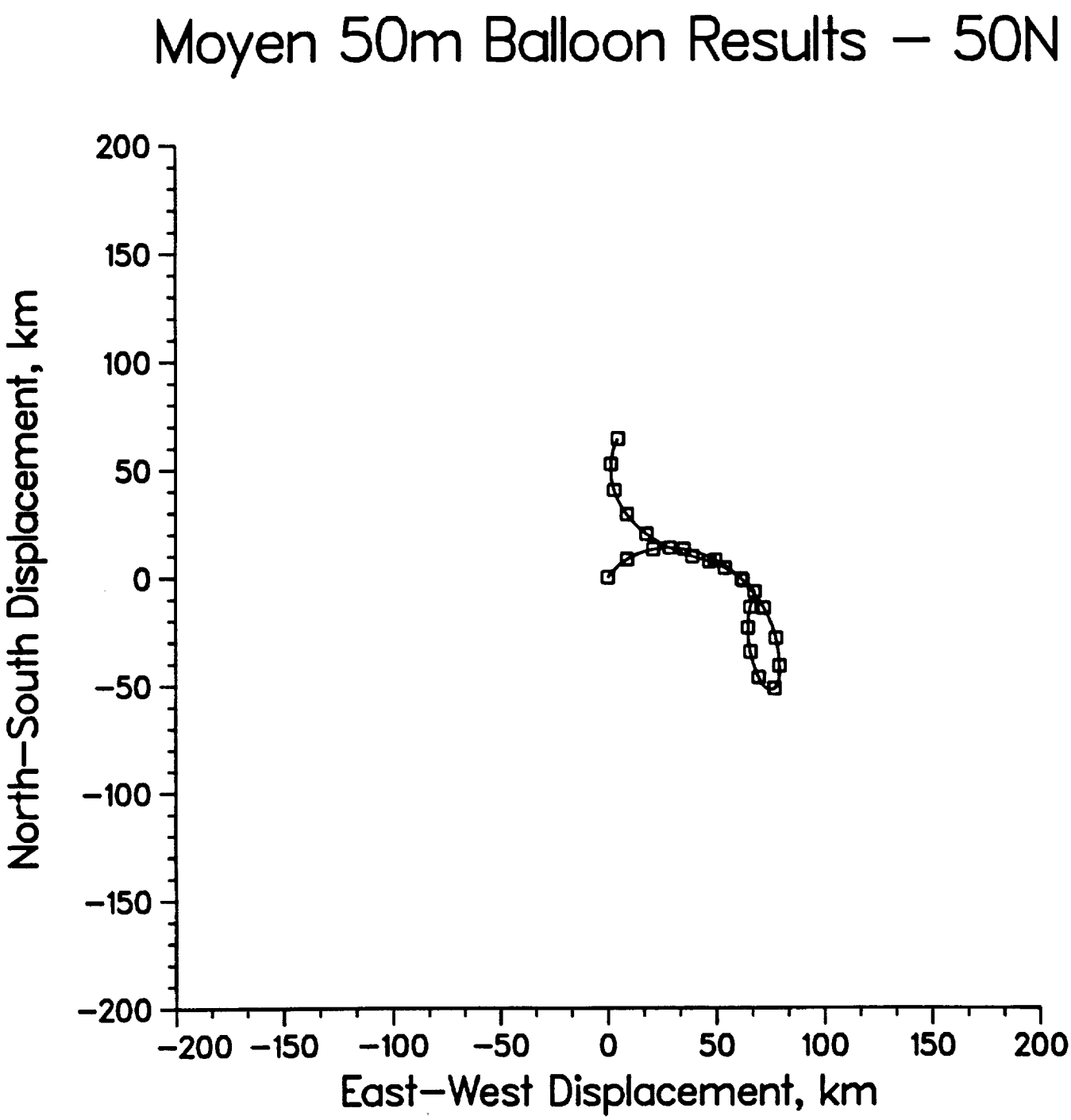
Moyen 50m Balloon Results – 50N
North–South Displacement, km
200
150
100
50
0
–50
–100
–150
–200
–200 –150 –100 –50 0 50 100 150 200
East–West Displacement, km

Figure 3.

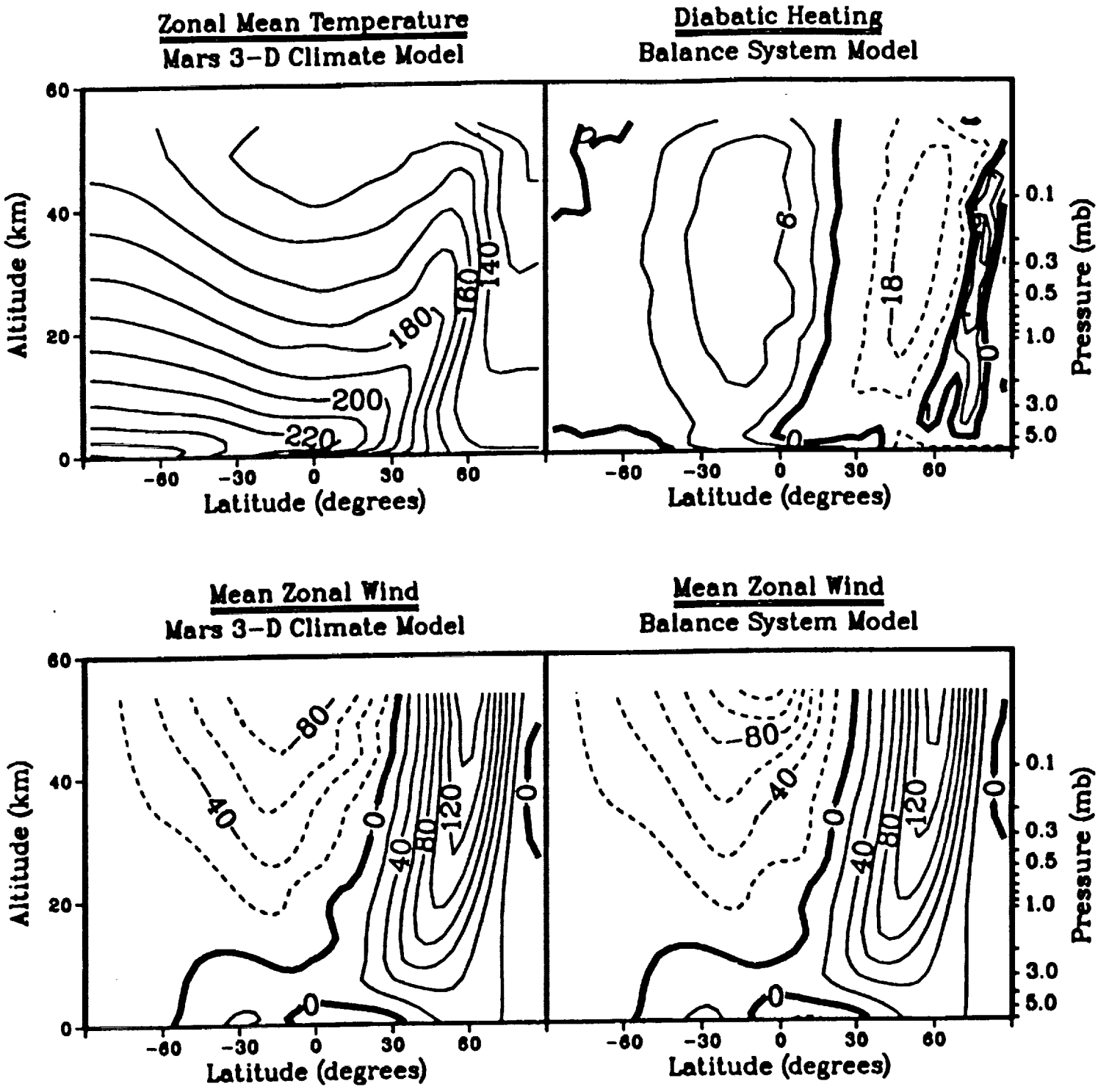
Zonal Mean Temperature
Mars 3-D Climate Model
Diabatic Heating
Balance System Model
Mean Zonal Wind
Mars 3-D Climate Model
Mean Zonal Wind
Balance System Model
Altitude (km)
Pressure (mb)
Latitude (degrees)
60
40
20
0
-60
-30
0
30
60
0.1
0.3
0.5
1.0
3.0
5.0
140
160
180
200
220
-18
-8
-80
-40
40
80
120

Figure 4.

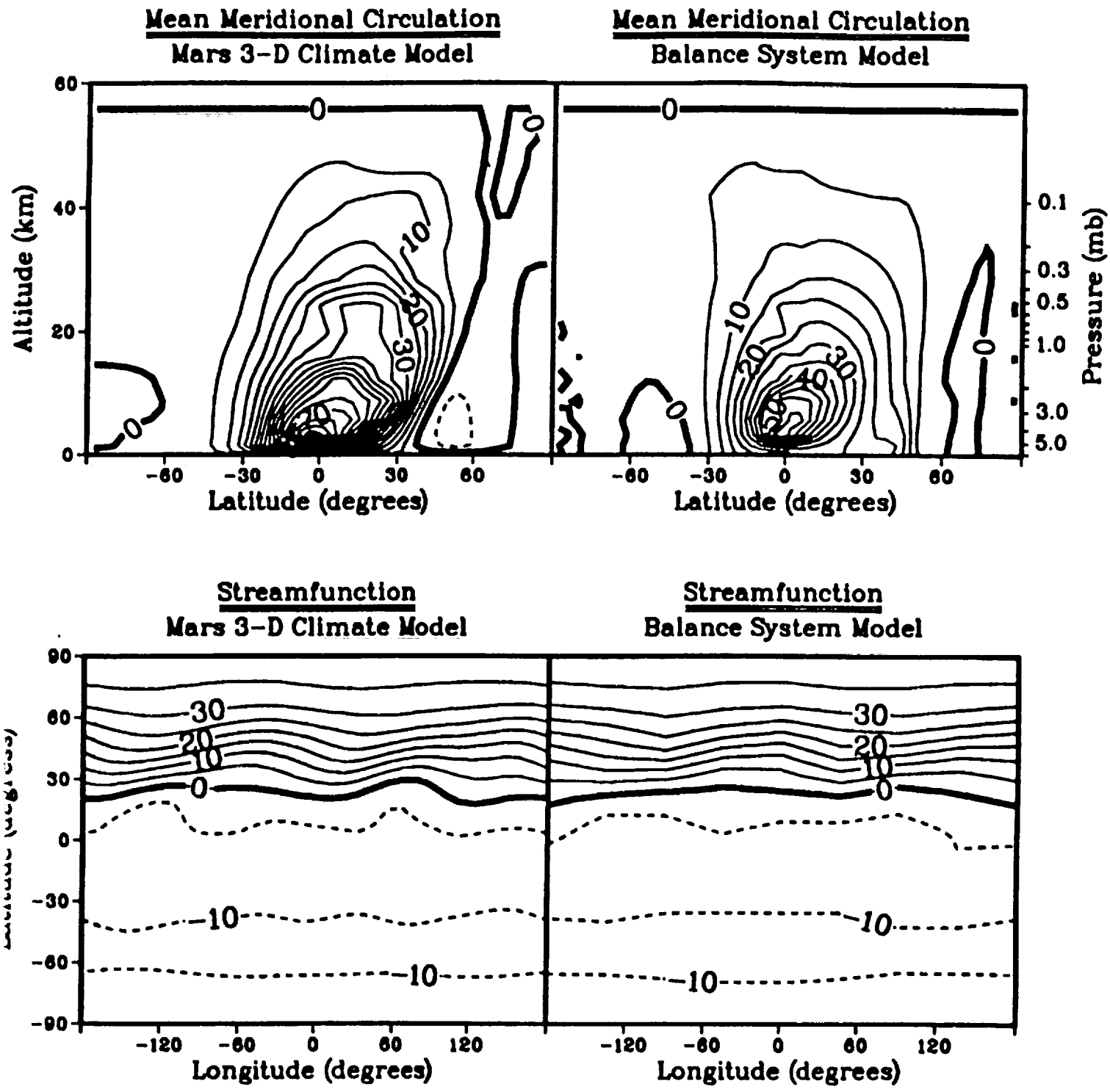
Mean Meridional Circulation
Mars 3-D Climate Model
Mean Meridional Circulation
Balance System Model
Altitude (km)
Pressure (mb)
Latitude (degrees)
Latitude (degrees)
Streamfunction
Mars 3-D Climate Model
Streamfunction
Balance System Model
Longitude (degrees)
Longitude (degrees)

Figure 5.

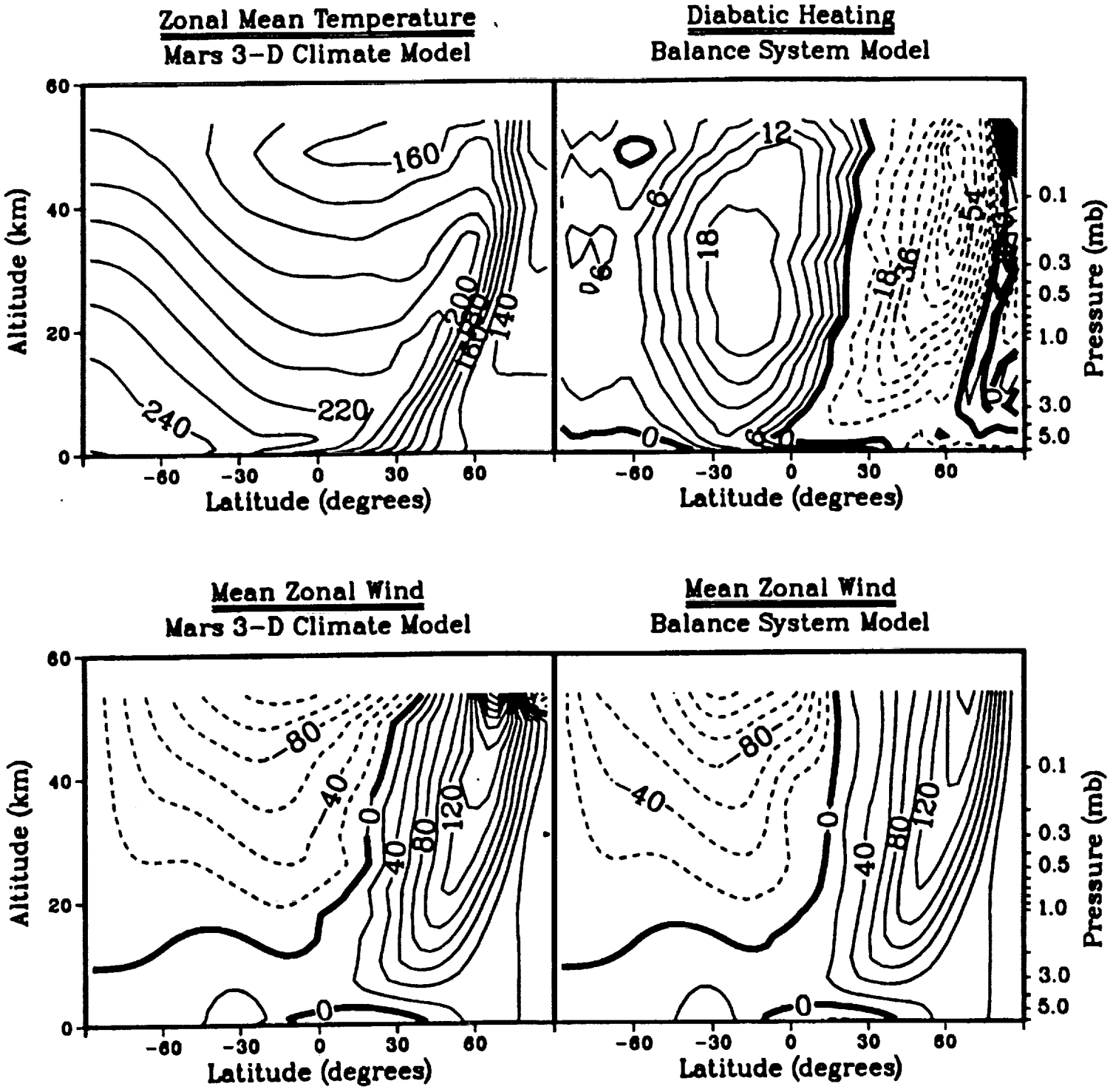
Zonal Mean Temperature
Mars 3-D Climate Model
Diabatic Heating
Balance System Model
Altitude (km)
Pressure (mb)
Latitude (degrees)
160
200
180
140
220
240
12
6
18
36
54
0
Mean Zonal Wind
Mars 3-D Climate Model
Mean Zonal Wind
Balance System Model
80
40
120

Figure 6.

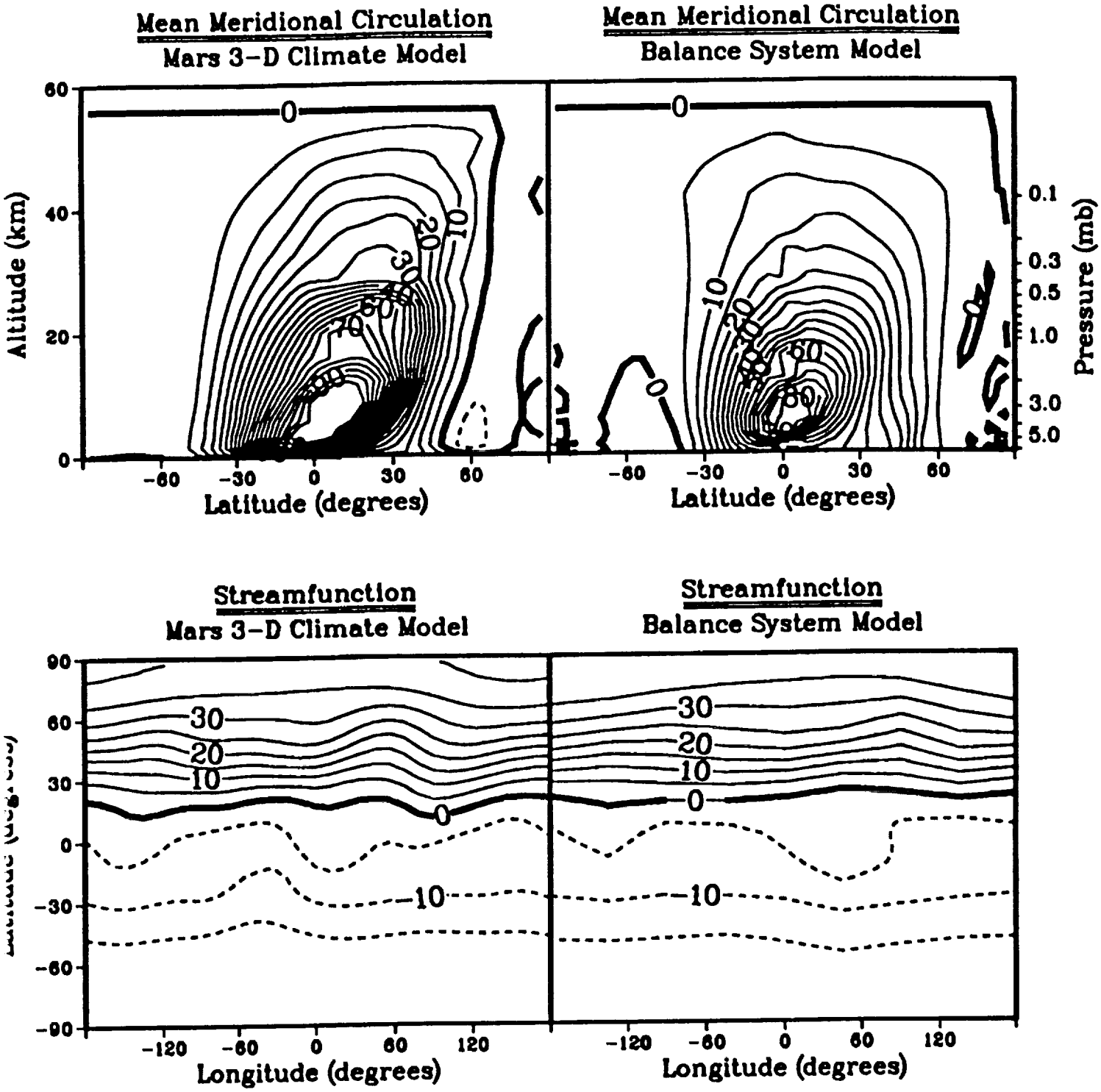
Mean Meridional Circulation
Mars 3-D Climate Model
Mean Meridional Circulation
Balance System Model
Altitude (km)
Pressure (mb)
Latitude (degrees)
Latitude (degrees)
Streamfunction
Mars 3-D Climate Model
Streamfunction
Balance System Model
Longitude (degrees)
Longitude (degrees)

Figure 7.

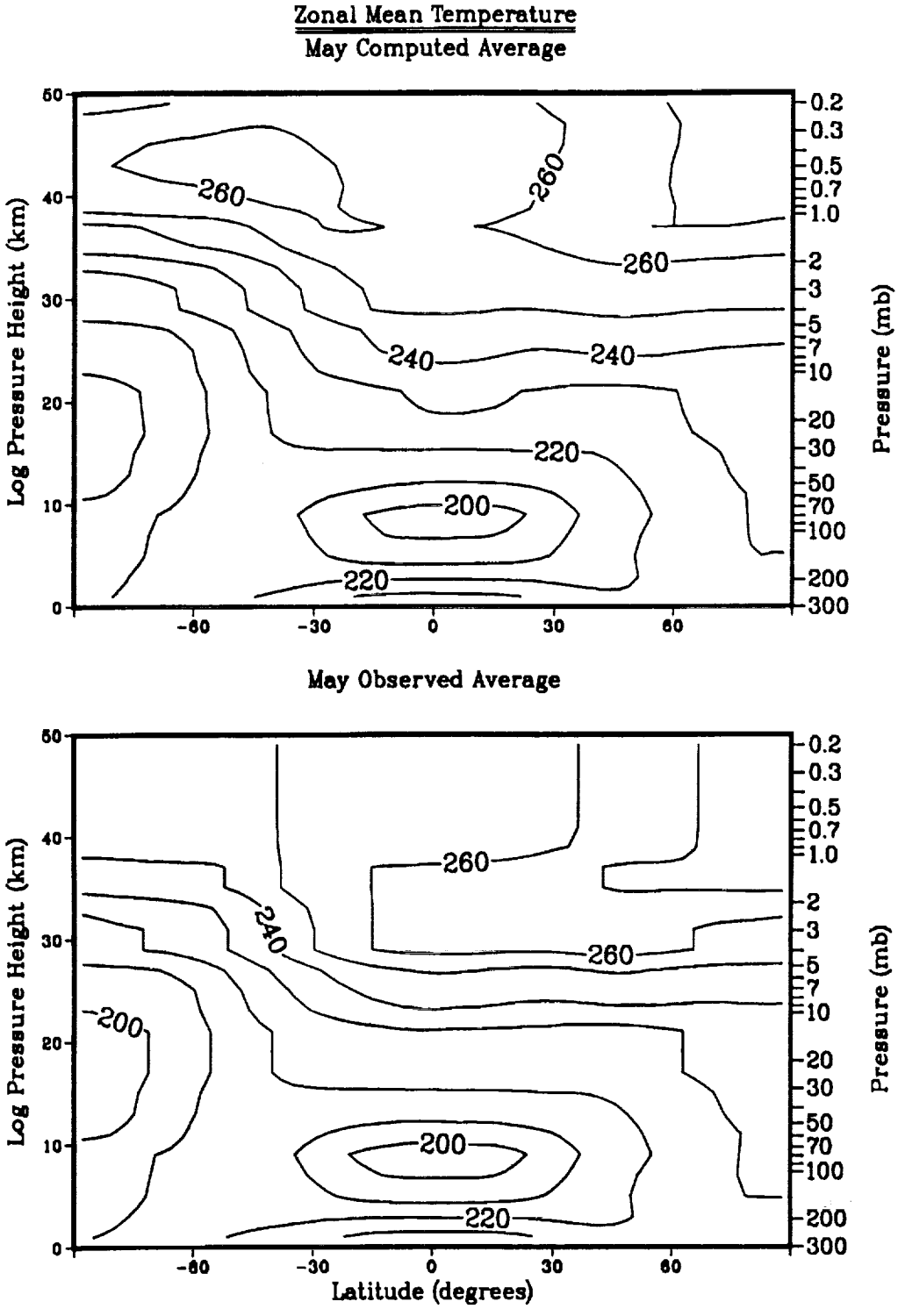
Zonal Mean Temperature
May Computed Average
Log Pressure Height (km)
Pressure (mb)
260
240
220
200
May Observed Average
Latitude (degrees)

Figure 8.

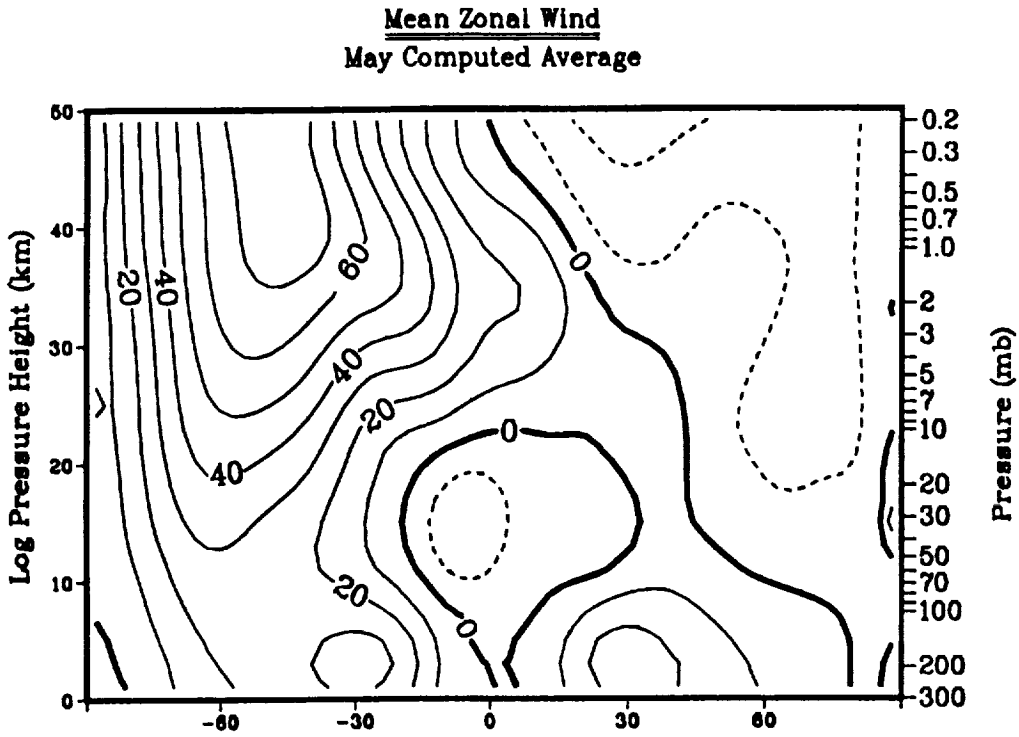
Mean Zonal Wind
May Computed Average
Log Pressure Height (km)
Pressure (mb)
60
40
30
20
10
0
-60
-30
0
30
60
0.2
0.3
0.5
0.7
1.0
2
3
5
7
10
20
30
50
70
100
200
300
-20
-40
-60
40
20
0

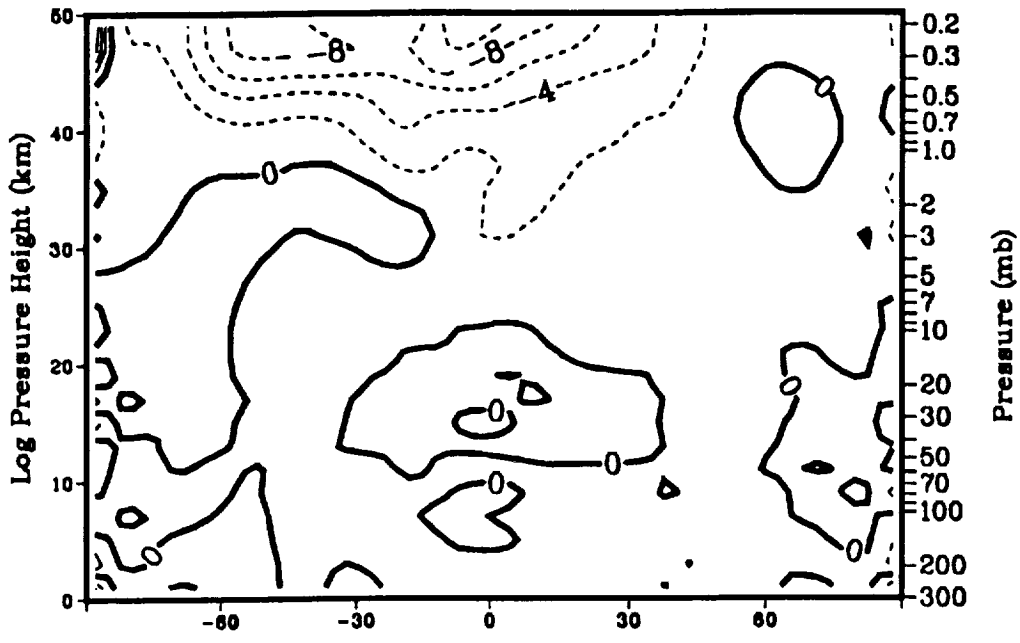
Mean Meridional Wind
May Computed Average
Log Pressure Height (km)
Pressure (mb)
60
40
30
20
10
0
-60
-30
0
30
60
0.2
0.3
0.5
0.7
1.0
2
3
5
7
10
20
30
50
70
100
200
300
-8
-4
0

Figure 9.

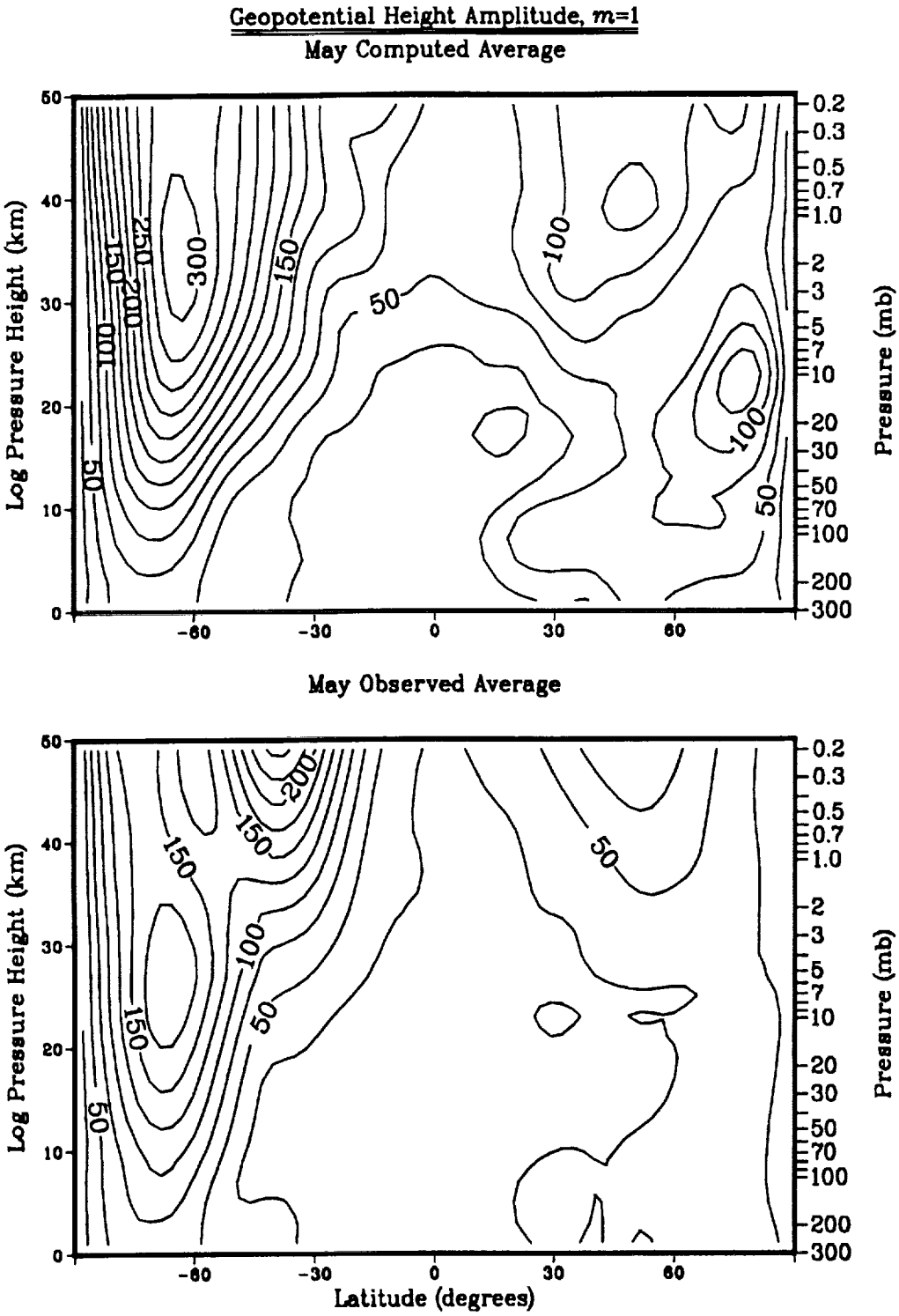
Geopotential Height Amplitude, m=1
May Computed Average
Log Pressure Height (km)
Pressure (mb)
May Observed Average
Latitude (degrees)

Figure 10.

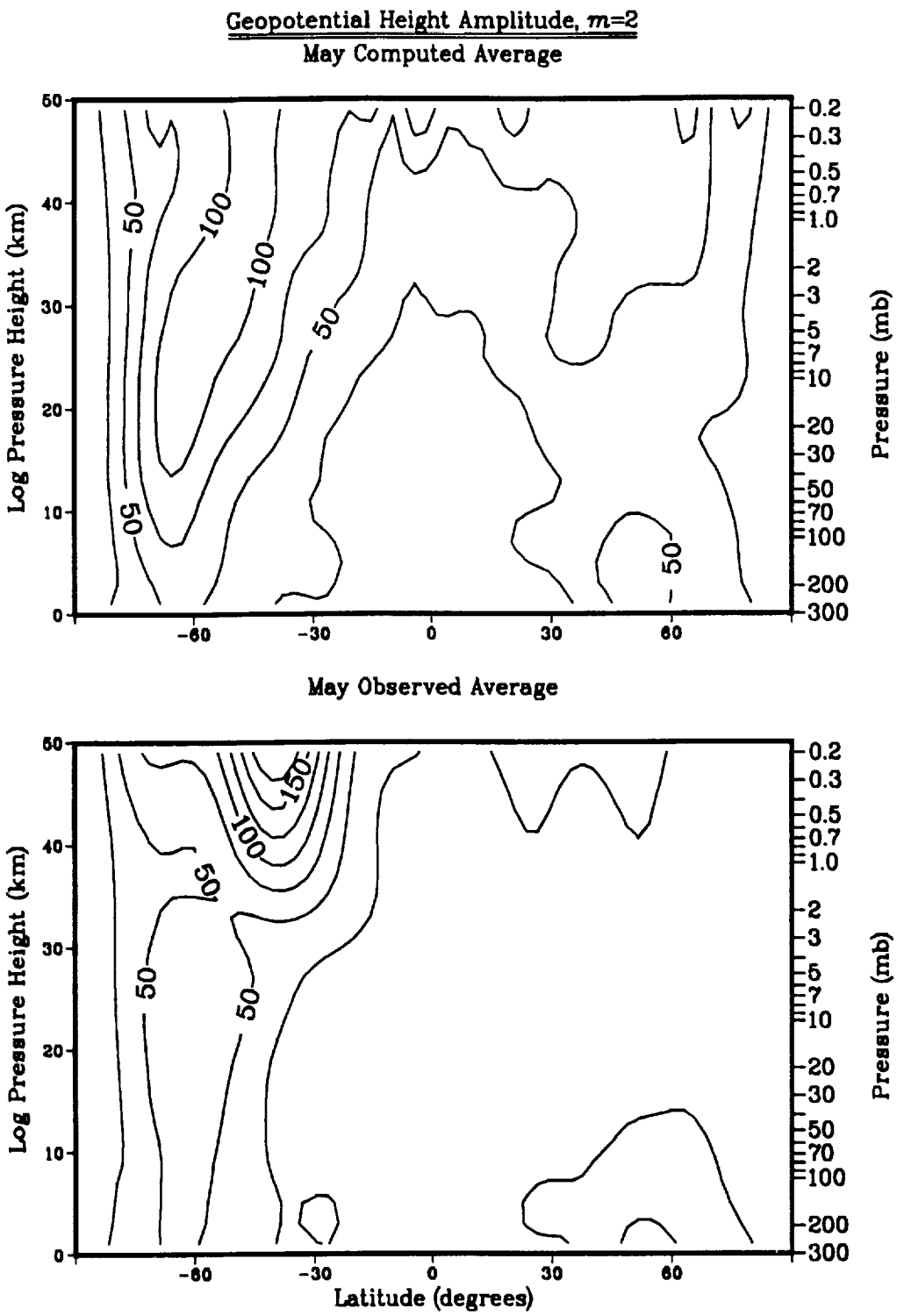
Geopotential Height Amplitude, m=2
May Computed Average
Log Pressure Height (km)
Pressure (mb)
50
100
100
50
50
50
0.2
0.3
0.5
0.7
1.0
2
3
5
7
10
20
30
50
70
100
200
300
0
10
20
30
40
50
-60
-30
0
30
60
May Observed Average
Log Pressure Height (km)
Pressure (mb)
150
100
50
50
50
Latitude (degrees)

Figure 11.

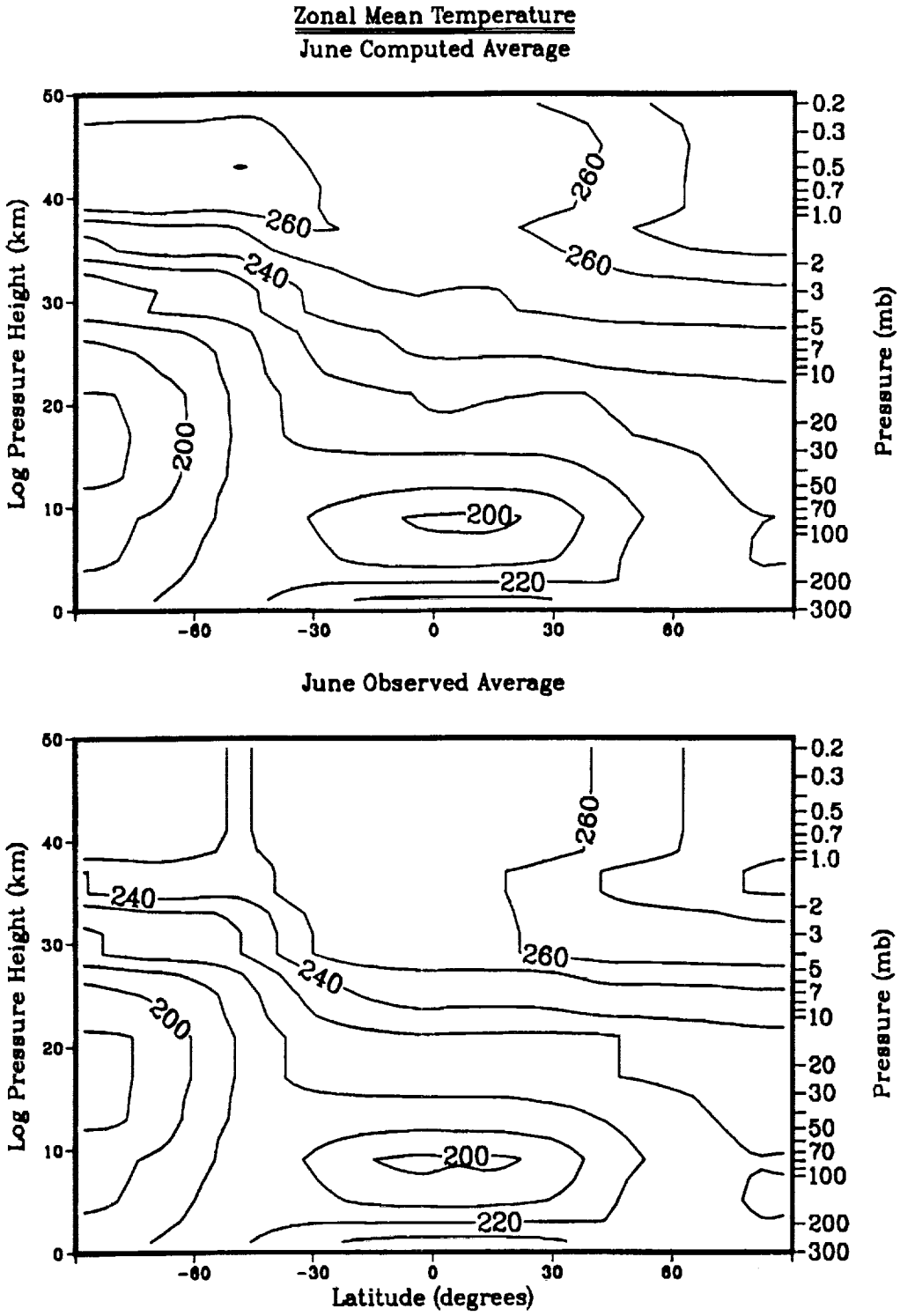
Zonal Mean Temperature
June Computed Average
Log Pressure Height (km)
Pressure (mb)
260
240
200
220
June Observed Average
Latitude (degrees)

Figure 12.

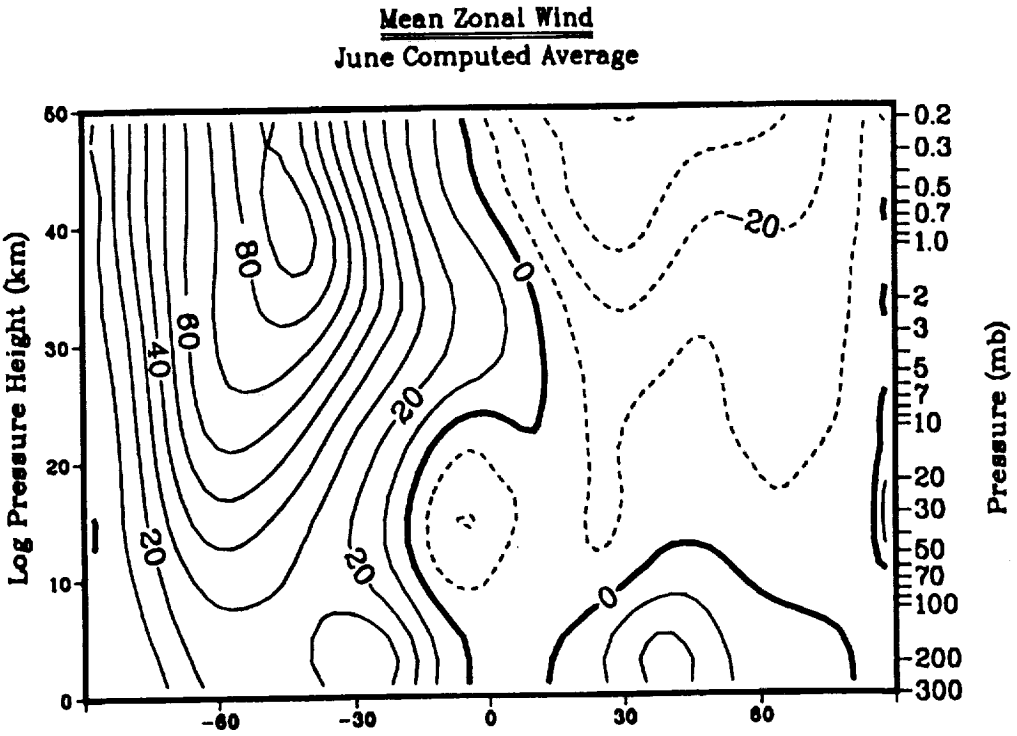
Mean Zonal Wind
June Computed Average
Log Pressure Height (km)
Pressure (mb)
80
60
40
20
0
-20
-60
-30
0
30
60
0.2
0.3
0.5
0.7
1.0
2
3
5
7
10
20
30
50
70
100
200
300

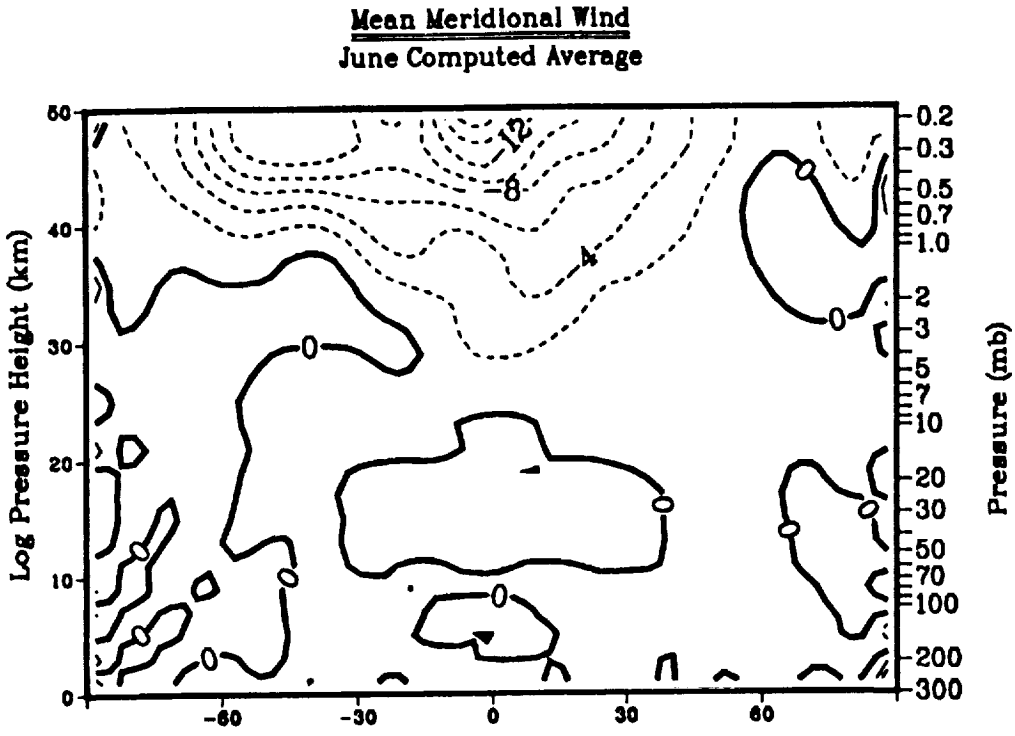
Mean Meridional Wind
June Computed Average
Log Pressure Height (km)
Pressure (mb)
12
8
4
0
-60
-30
0
30
60
0.2
0.3
0.5
0.7
1.0
2
3
5
7
10
20
30
50
70
100
200
300

Figure 13.

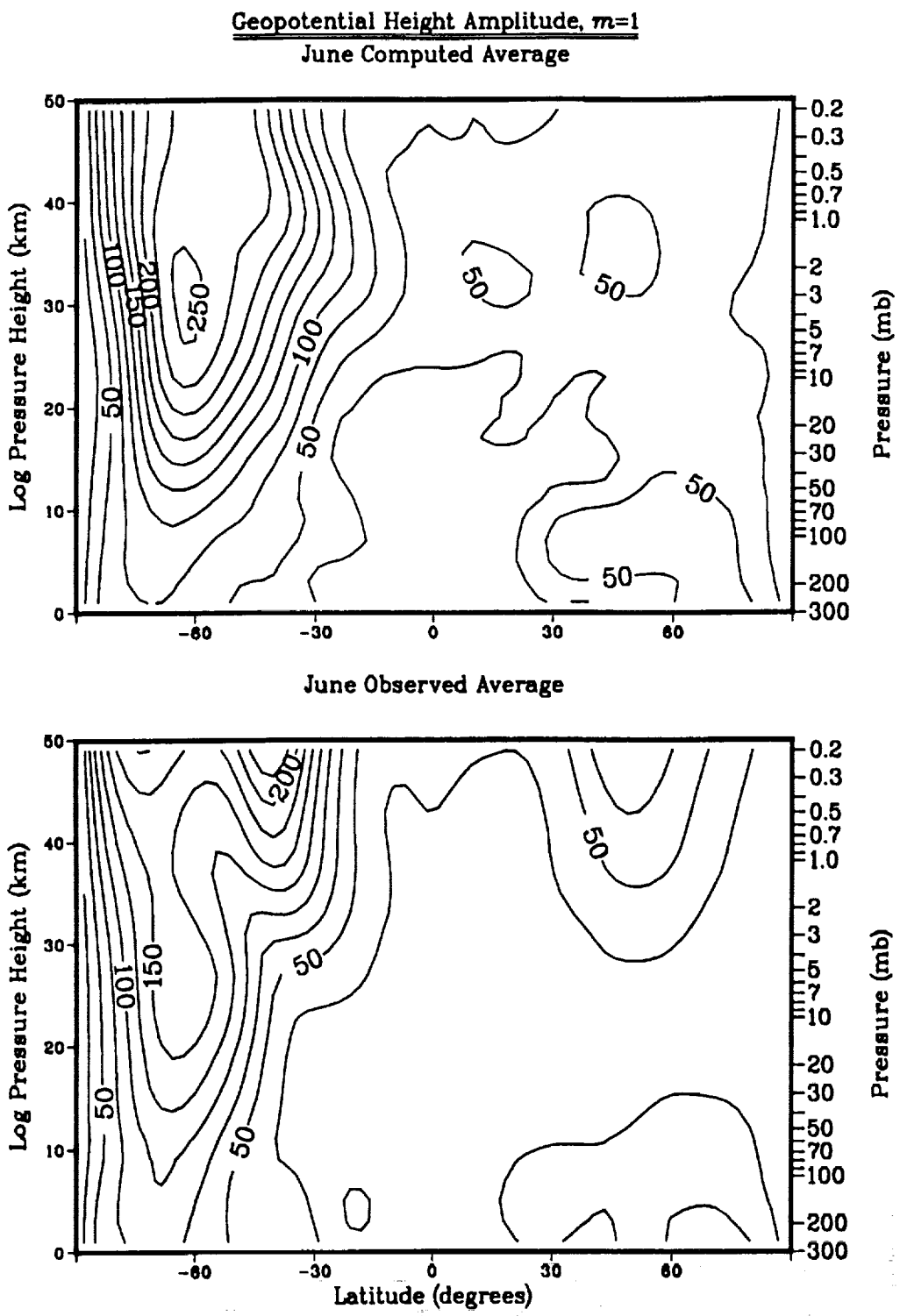
Geopotential Height Amplitude, m=1
June Computed Average
Log Pressure Height (km)
Pressure (mb)
50
100
150
200
250
50
50
50
50
50
June Observed Average
Log Pressure Height (km)
Pressure (mb)
200
50
150
100
50
50
Latitude (degrees)

Figure 14.

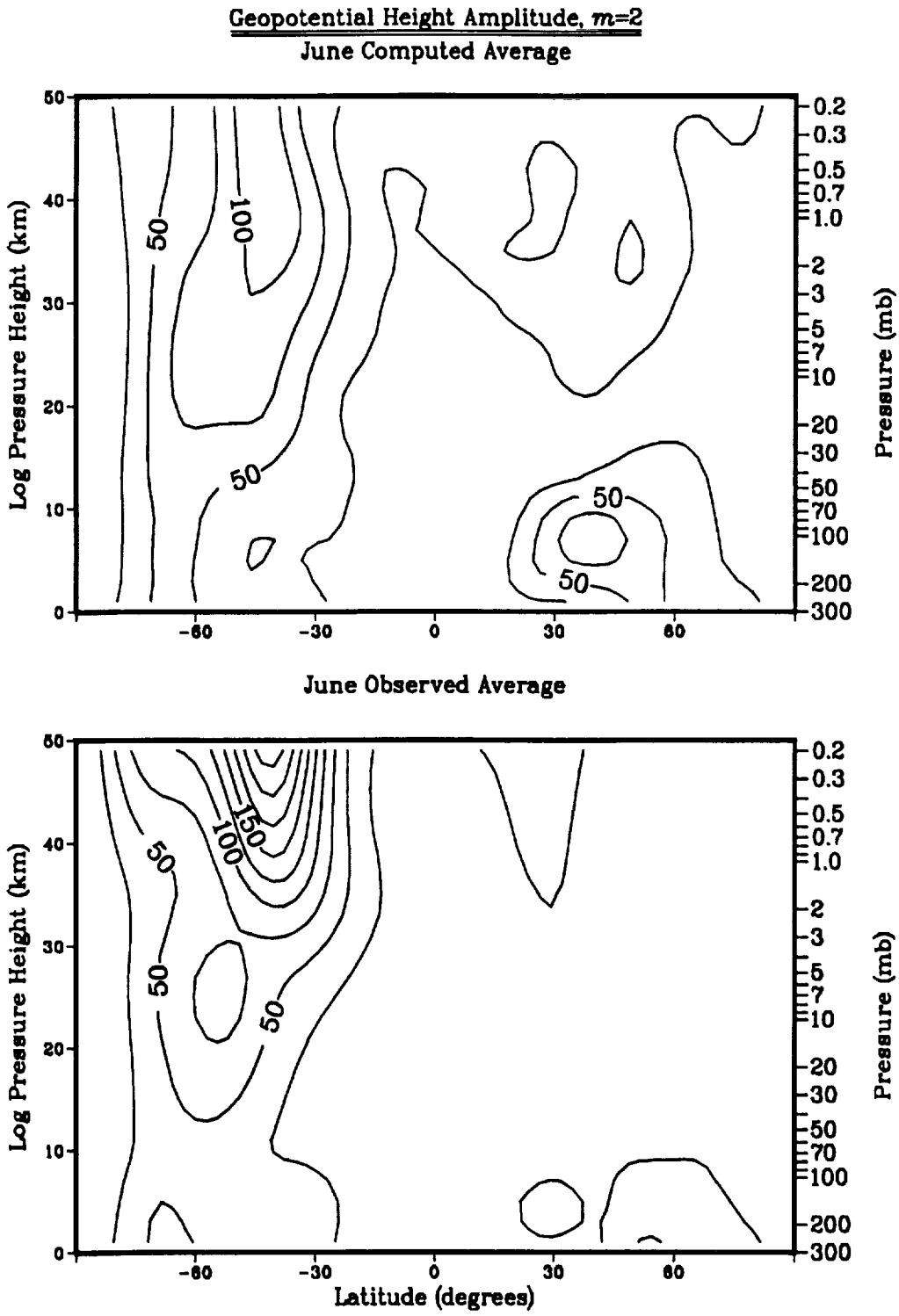
Geopotential Height Amplitude, m=2
June Computed Average
Log Pressure Height (km)
Pressure (mb)
50
100
50
50
50
0.2
0.3
0.5
0.7
1.0
2
3
5
7
10
20
30
50
70
100
200
300
-60
-30
0
30
60
June Observed Average
Log Pressure Height (km)
Pressure (mb)
150
100
50
50
50
Latitude (degrees)

Figure 15.

A COUPLED SUBSURFACE ATMOSPHERE BOUNDARY LAYER MODEL OF H_2O ON MARS

A. P. Zent, SETI Institute and NASA Ames Research Center, R. H. Haberle, NASA Ames Research Center, Moffett Field, Ca 94035, H. Houben, Space Physics Research Institute, Sunnyvale, Ca. 94087, B. M. Jakosky, LASP, University of Colorado, Boulder, Co. 80309.

We have developed a coupled subsurface-atmosphere boundary layer model of H_2O exchange on Mars. Our objectives in constructing this model are: a) to identify the physical processes that control exchange of water between the atmosphere and regolith over a diurnal timescale on Mars, and to define physical parameters that can be used predictively; b) to understand the intensity as well as temporal and spatial variability of the H_2O flux through the martian surface; c) to develop a description of how exchange patterns vary throughout reasonable parametric space; and d) to advance our understanding of the martian annual H_2O cycle.

Model: The atmospheric boundary layer model is taken from Haberle *et al.*51990, and is described in detail by those authors. It is a radiative-convective model which allows for the radiative effects of dust. The model is similar to that by Flasar and Goody (1976), however the model has an improved treatment of turbulence, and provides a self-consistent calculation of surface stresses, which help regulate the exchange of water between the surface and atmosphere.

The subsurface model consists of a thermal component and a H_2O transport component. The heat conduction equation was solved in order to find subsurface temperatures. Viking data was used to constrain the thermal constants. Boundary conditions are found from the atmosphere model, which calculates the radiative and sensible heat fluxes. The surface temperature is then calculated assuming that the radiative, sensible, conductive, and latent heat fluxes sum to zero. The lower boundary condition is found by extending the solution region obtained to depths greater than the penetration depth of the annual thermal wave. The thermal gradient at the lower boundary is then assumed to be the quotient of the heat flux, calculated assuming a chondritic Mars, and the conductivity.

There are four assumptions that underlie the model of H_2O transport through the regolith. The first is that vertical transport of H_2O through the regolith is according to Fick's law. We further assume that water in the regolith must exist in one of three discrete states, either as vapor, adsorbate, or ice.

$$\sigma = f\gamma + \alpha(\gamma, T) + \iota \tag{1}$$

Where σ is the total density of water per cubic meter of regolith, f is the porosity of the regolith, γ is the vapor density per cubic meter of *gas*, α is the adsorbed phase, and ι is the ice phase.

Some assumption must be made regarding the form of the expression $\alpha(\gamma, T)$. Our third assumption is that

$$\alpha(\gamma, T) = \frac{\beta P^{0.51}}{exp(\delta/T)} \tag{2}$$

Where $\beta = 2.043 \times 10^{-8}$, and δ is -2679.8 (Fanale and Cannon, 1971). P is the partial pressure of H_2O , leading to our final assumption, that the ideal gas law is obeyed by H_2O .

The evolution of the population in a finite volume of regolith is controlled by

$$\frac{d\sigma}{dt} = \frac{d\phi}{dz} = \frac{\partial}{\partial z} D \frac{\partial \gamma}{\partial z} \tag{3}$$

Where σ is the total concentration of H_2O in the regolith, γ is the vapor phase concetration, and ϕ is the flux. The upper boundary condition is a flux, which is calculated by assuming that the vapor pressure of H_2O at the mathematical surface is controlled by adsorption. That permits the atmosphere layer model to calculate a gradient and resulting flux through the surface via stability functions from Monin-Obukhov similarity theory. The lower boundary condition for H_2O is zero flux.

The model is initialized with no H_2O in the atmosphere and 2.1 kg m^{-3} throughout the regolith. We carry out the calculation until the day to day variation of H_2O in the atmosphere column is less than 0.01%. Accordingly, the atmospheric H_2O column is stable over a timescale longer than the diurnal radiation pattern remains constant. We note that equilibration typically

requires 12 to 18 sols, providing the first estimate of the timescale for the atmosphere and regolith to equilibrate.

Results: As our baseline case, we take the latitude and season that the Viking One lander touched down; albedos and thermal inertias are consistent with the Viking data.

Beginning at midnight, the atmosphere is quite stable, the only turbulence is due to wind shear (Fig. 1). The regolith cools progressively throughout the night, increasing its adsorptive capacity (Eq. 2 and Fig. 2). The water vapor mixing ratio in the lower part of the atmosphere decreases as the night progresses because the cooling regolith is scavenging H_2O ; due to the stability of the atmosphere, supply of water to the regolith is effectively diffusion limited.

Sunrise occurs just before 0600 hours, and the soil begins to warm. Although the atmosphere is not yet convective, there is a thin layer of atmospheric mixing that brings additional water down to the surface, where the warming regolith continues to adsorb more water. Although physical adsorption is inhibited at higher temperatures, we predict continued adsorption after sunrise because the regolith is not in equilibrium with the atmosphere as a whole, but only with the strongly depleted lowest tens of meters.

Even after the atmosphere becomes fully convective, about 0800 hours, there is still a short period where the atmosphere is supplying water to the regolith. The flux *into* the soil increases dramatically when the atmosphere begins to convect freely (Fig. 3). It isn't until about 1000 hours that the increasing temperature and adsorbed water content raise the pore pressure of water to atmospheric levels and the flux reverses.

During the day the atmosphere is fully convective, and there is only a very shallow vertical gradient in atmospheric water. The regolith communicates during the day with the entire boundary layer, and approximate equilibrium exists. Even before the surface temperature peaks, the flux to the atmosphere begins to drop as the amount of near-surface H_2O is depleted. Again in the late afternoon, there is a strong pulse of H_2O *into* the regolith, as the atmosphere is still convecting vigorously, but the regolith is now cooling rapidly. Finally, once the surface cools below the temperature of the atmosphere, about 1650 hours, convection stops, the atmosphere stabilizes, and the slow scavenging of H_2O from the lowest tens of meters of the atmosphere begins again.

We have examined the effects of albedo, thermal inertia, latitude, atmospheric optical depth, and pore size on our baseline model, and will report those results as time permits.

Fanale, F. P. and Cannon, W. 1971, *Nature* **230** 502 -504.
Flasar, F. M. and R. M Goody, 1976, Planet Space Sci. **24**, 161-181.
Haberle *et al.* 1990, Submitted J. Atmos. Sci.

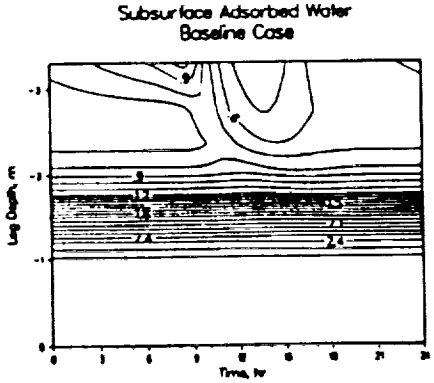

Figure 2. Subsurface adsorbed water profile vs. time.

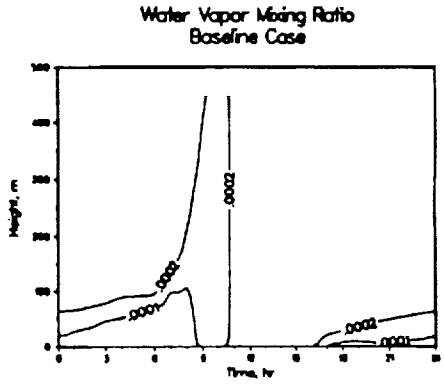

Figure 1. Atmospheric water vapor mixing ratio vs time.

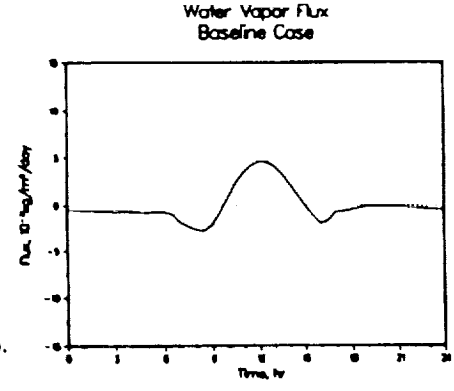

Figure 3. H_2O flux vs. time. Flux greater than zero is up.